Different Supercapacitive Behavior of Two Glucose-derived Microporous Carbons: Direct Pyrolysis versus Hydrothermal Carbonization

Marta Sevilla,*[a] Linghui Yu,[b,c] Conchi O. Ania,[a] Maria-Magdalena Titirici*[d]

Abstract

This work compares for the first time the physical and chemical characteristics of activated carbons produced from glucose and hydrothermally carbonized glucose, as well as their performance as electrodes in supercapacitors in aqueous electrolyte (H_2SO_4). Both KOH-activated carbons exhibit similar textural properties, with BET surface areas of ~ 1400-1500 m^2/g and a pore volume of ~ 0.70 cm^3/g, the pore size distribution being centered in the micropore range. When tested as supercapacitor electrodes, the activated carbon produced from hydrothermally carbonized glucose exhibits a superior rate capability due to lower EDR (being able to work at an ultra-high discharge current of 90 A/g), as well as higher specific capacitance (~ 240 F/g vs. ~ 220 F/g for glucose-derived activated carbon at 0.1 A/g). Both supercapacitors have excellent robustness, even for a large voltage cell of 1.2 V in 1 M H_2SO_4.

Keywords: energy storage; porosity; activation; hydrothermal carbonization

[a] *Dr. M. Sevilla, Dr. C. O. Ania. Instituto Nacional del Carbón (CSIC), P. O. Box 73, Oviedo 33080, Spain. Fax: (+34) 985297662. E-mail: martasev@incar.csic.es (M. Sevilla)*

[b] *Max-Planck Institute of Colloids and Interfaces, Am Muhlenberg 1, 14476, Potsdam, Germany*

[c] *School of Materials Science and Engineering, Nanyang Technological University, 50 Nanyang Avenue, Singapore 639798, Singapore*

[d] *Queen Mary, University of London, School of Engineering and Materials Science, Mile End Road, London, E1 4NS, United Kingdom. E-mail: m.m.titirici@qmul.ac.uk*

Introduction

Growing global concern for the security of the world's energy supply has spurred interest in further development of electric devices as source of power and energy, and as back-up for renewable sources. Among the different possibilities, electrochemical capacitors hold promise for load-leveling, energy recovering and peak-power supply. However, further breakthroughs in materials and electrolytes are essential to comply with the higher requirements of future systems. Cost reduction is also a critical element for their widespread commercialization.

Activated carbons continue to be the main choice electrode material in commercial devices owing to its large surface area, high chemical stability, fairly good electronic conductivity and relatively low cost. [1-3] Nevertheless, its performance in terms of capacitance value and capacitance retention needs to be further improved by advancements in porosity control through novel activation procedures, while keeping the cost to a low level.

Compared to conventional activated carbon precursors such as petroleum coke, coal and charcoal, biomass is more suitable in terms of availability, renewable nature and price. However, its non-uniform structure and mineral matter content are drawbacks for achieving uniform and reproducible properties of the produced activated carbons. Additionally, the low carbon yield when pyrolyzed, [4] decreases the efficiency of the process. In this regard, hydrothermal carbonization has stood out as a procedure for homogenizing biomass, while removing the mineral matter and increasing aromaticity of biomass and thereby the carbon yield. Recently, Sevilla *et al.* reported that the direct KOH activation of the microalgae *Spirulina platensis* leads to a complete burnout, whereas hydrothermally carbonized microalgae can be successfully converted into a highly microporous carbon with excellent CO_2 capture capacity.[5] The hydrothermal

carbonization process not only increases the carbon yield, but also partially removes the mineral matter contained in the microalgae; on the contrary, the solid-state pyrolysis process leas to the accumulation of the mineral matter in the solid product.[6]

Chemical activation with KOH of hydrothermal carbons derived from a variety of biomass has shown to be a powerful tool for the generation of highly microporous carbons with superior performance in gas (hydrogen storage,[7] CO_2 capture,[5, 8] methane storage [9]) and energy storage (supercapacitors) [10-14] owing to their controlled porous structure. In particular, for energy storage, activated carbons prepared from hydrothermally carbonized sawdust have shown excellent performance in organic electrolyte (1 M $TEABF_4$ in acetonitrile), with a specific capacitance of up to ~ 240 F/g (100 F/cm^3) at 0.1 A/g and ~ 70% capacitance retention at high discharge current, *i.e.* 20 A/g. Furthermore, such material outperformed by 100% a commercial activated carbon optimized for EDLC applications, *i.e.* YP-17D from Kuraray Chemicals. Very recently, Wang et al. showed superb capacitance retention (up to 100 A/g) in an ionic liquid electrolyte for carbon nanosheets obtained by activation of hydrothermally carbonized hemp. [14]

Several groups, including ours, have previously compared the chemical structure and physical properties of carbohydrate-derived carbon materials directly pyrolyzed and firstly hydrothermally treated and then pyrolyzed. [15-17] There is a lot of interest in understanding the chemical and structural differences as a key element for several applications including heterogeneous catalysis,[18, 19] energy storage [20] as well as biochar in soil applications. [21]

Herein we compare for the first time in the literature the physical and chemical characteristics of activated carbons produced from glucose and hydrothermally carbonized glucose, as well as their performance as electrodes in supercapacitors

working with H_2SO_4. Both two and three-electrode measurements were performed in order to fully characterize the electrochemical behavior of the materials.

Results and Discussion

Chemical and structural characteristics

The morphology and size of the carbon particles was examined by scanning electron microscopy (SEM). As shown in Figure 1, ACG is composed of relatively small particles (< 10 μm) of irregular morphology, while ACHG is made up of large particles (> 100 μm) with conchoidal cavities, morphology already observed for other activated carbons derived from hydrothermally carbonized biomass. [5, 7] Even though the particles are much bigger in ACHG than in ACG, those conchoidal cavities may ensure the rapid transport of species into the bulk of the particles.

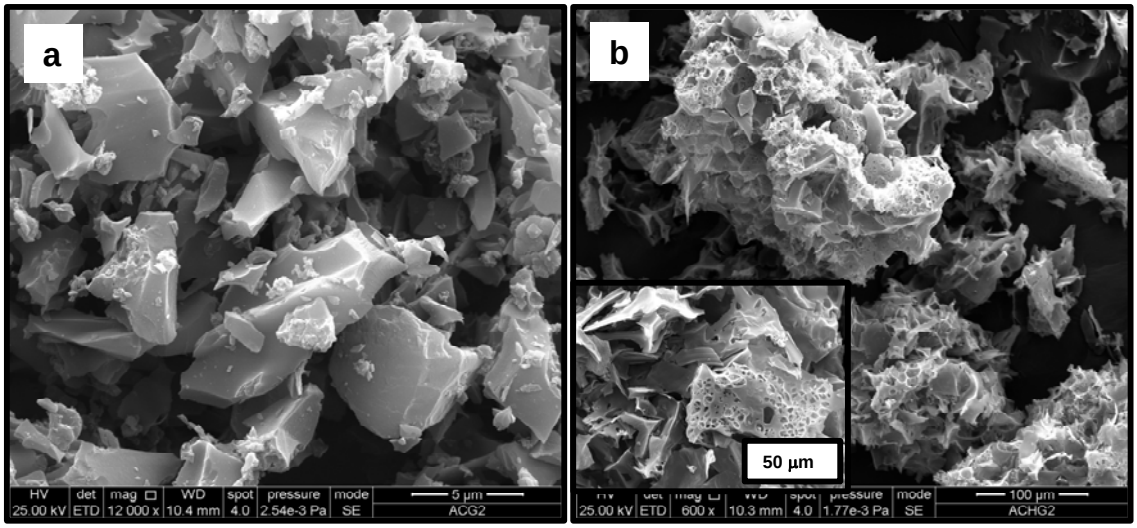

Figure 1. SEM images of ACG (a) and ACHG (b).

As evidenced by the N_2 physisorption isotherms depicted in Figure 2a, the activated carbons obtained for both glucose and hydrothermally carbonized glucose are highly microporous. Thus, a sharp knee is observed for relative pressures below 0.05 and a

horizontal plateau for higher relative pressures, which is indicative of a narrow pore size distribution centered in the micropore range. This is confirmed by the NLDFT PSDs shown in Figure 2b, where no pores larger than 2 nm can be detected for ACHG and only a small fraction of pores up to 3 nm in ACG. In fact, as shown by the pore volumes determined by CO_2 adsorption (see Table 1) and the NLDFT PSD derived from CO_2 adsorption (Figure 2b), most of the porosity of these porous carbons corresponds to narrow microporosity, *i.e.* pore size < 0.7 nm. Indeed, the average micropore width determined by applying the Dubinin-Radushkevich equation to the N_2 adsorption data is 0.7 nm for ACHG and 0.9 nm for ACG. Both samples exhibit thereby similar textural characteristics, with a BET surface area of ~ 1400-1500 m^2/g and a pore volume of ~ 0.70 cm^3/g (Table 1).

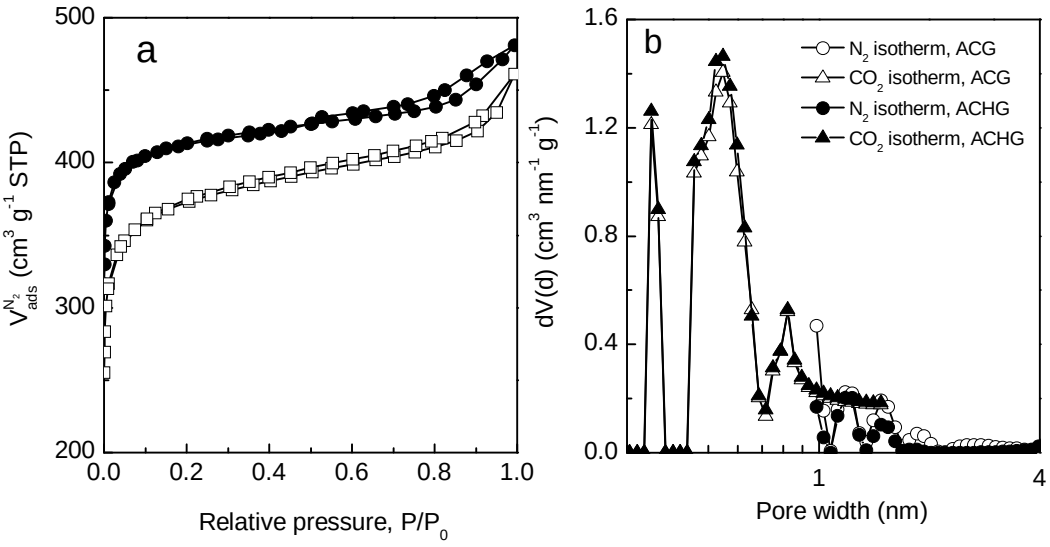

Figure 2. N_2 physisorption isotherms at 77K (a) and NLDFT pore size distributions of ACG and ACHG (b). In Figure (a), the isotherm of ACHG has been up-shifted by 30 cm^3 g^{-1}.

Table 1. Textural and chemical characteristics of the porous carbons.

Sample	S_{BET} ($m^2\ g^{-1}$)	V_p[a] ($cm^3\ g^{-1}$)	V_0 (N_2)[b] ($cm^3\ g^{-1}$)	V_0 (CO_2)[c] ($cm^3\ g^{-1}$)	O (wt.%)	C (wt.%)	pH_{PZC}
ACG	1440	0.67	0.57	0.54	13.8	84.4	4.3
ACHG	1510	0.68	0.60	0.57	10.2	88.6	5.0

[a] Total pore volume determined at $P/P_0 \sim 0.95$. [b] Micropore volume determined by using the Dubinin–Radushkevich equation applied to the N_2 adsorption isotherm. [c] Micropore volume determined by using the Dubinin–Radushkevich equation applied to the CO_2 adsorption isotherm.

From a bulk chemical analysis point of view, both samples are also quite similar (see Table 1), though ACHG exhibits a higher carbon content and lower oxygen content (O/C weight ratio of 0.163 for ACG and 0.115 for ACHG), in line with the composition of the corresponding precursors (O/C weight ratio of 1.33 for glucose and 0.34 for hydrothermally carbonized glucose). Both samples have a slightly acidic character as inferred from the pH_{PZC} values.

The nature of the O-containing functionalities present in these materials was analyzed by means of temperature programmed desorption experiments (TPD). The CO and CO_2 desorption profiles are shown in Figure 3. In both cases, the amount of CO-desorbing groups is much larger than that of CO_2-desorbing groups (2.8 and 3.2 times higher for ACG and ACHG respectively), as is expected for carbon materials synthesized at 750 ºC. The lower value of the ratio CO/CO_2 evolved for ACG in comparison to ACHG agrees with its lower pH_{PZC}, confirming its slightly higher acidic character. On the other hand, the shape of the CO and CO_2 profiles is completely different, which points out clear chemical differences between the samples. Thus, ACG exhibits a sharp peak at around 310 ºC in both CO and CO_2 profiles (see Figure 3a), which is ascribed to carboxylic anhydrides, which decompose by releasing one CO and

one CO_2 molecule.[22, 23] That very well-defined peak tails a bit towards lower temperatures in the CO_2 desorption profile, suggesting the presence of a small amount of carboxylic acids and towards higher temperatures, indicating the presence of lactone groups. In the CO desorption profile, the sharp peak corresponding to the decomposition of anhydrides is accompanied by a broad peak centered at ~ 630 ºC, which is ascribed to phenols. On the contrary, for ACHG the CO_2 profile is broader, suggesting the presence of a variety of CO_2-desorbing groups with different chemical environments and thus varied thermal stability (see Figure 3b). Thereby, the CO_2 desorption profile can be deconvoluted into a first peak at around 250 ºC corresponding to carboxylic acids, a second one at 330 ºC attributed to carboxylic anhydrides (which has its counterpart in the CO desorption profile) and a broad peak centered at ~ 500ºC which is ascribed to lactone groups. Regarding the CO desorption profile, apart from the small lactone contribution, two peaks at around 640 and 810 ºC can be identified. They are attributed respectively to phenols and quinones/carbonyls.[22, 23] The latter moiety is well-known for giving rise to pseudocapacitance owing to the quinone/hydroquinone redox pair.[24] Meanwhile, high-polarity oxygen groups such as carboxyl and anhydride (which hydrolyze to carboxyl in aqueous medium) may hinder the motion of ionic species, increasing the resistance and causing capacitance fading with the increase of the current density.[24, 25]

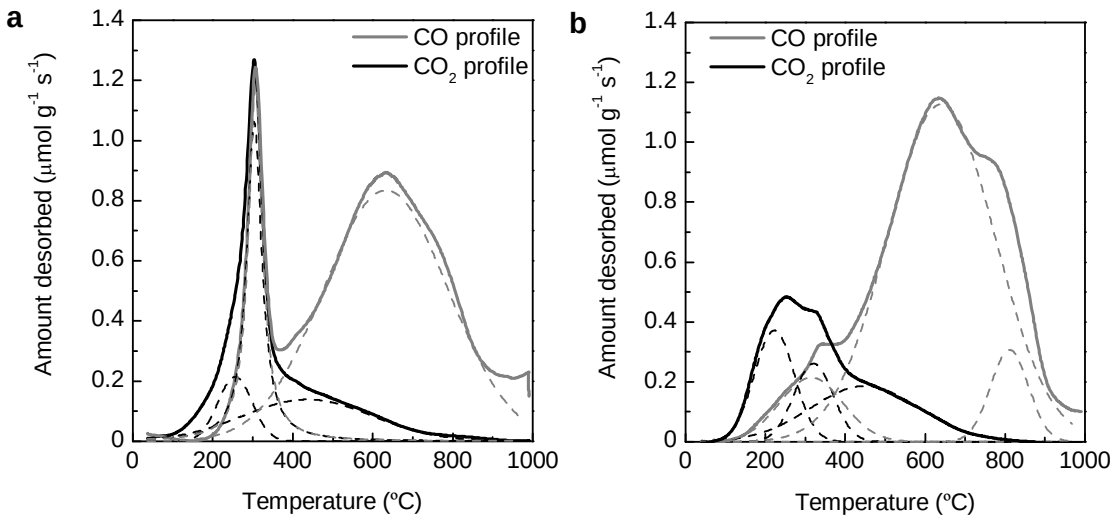

Figure 3. CO and CO_2 desorption profiles (including their deconvolution) for ACG (a) and ACHG (b).

It is important to mention that the product yield in the activation process is quite different, the one for the sample hydrothermally carbonized being significantly higher (55 %) as compared with the sample of glucose directly pyrolyzed (25 %) owing to the more aromatic structure of the former as a result of the hydrothermal carbonization process.[6, 15, 26] This result is meaningful as it implies that a lower amount of precursor is needed during the activation process in order to get a significant amount of final product and therefore a lower amount of corrosive KOH. On the other hand, for higher activation temperatures or KOH/precursor ratios, the amount of activated carbon obtained from glucose is negligible or null, whereas a yield = 30 % is achieved, for example, for a KOH/HTC carbon ratio = 4 and T = 750ºC. As previously shown for other kinds of biomass,[5] the hydrothermal carbonization step is key for the successful conversion of biomass into an advance porous carbon.

Supercapacitor performance

Both 3- and 2-electrode cell measurements in 1 M H_2SO_4 were performed on the activated carbons prepared from pristine glucose and hydrothermally carbonized glucose. While the 3E cell configuration is useful for studying the electrochemical behavior of a material, the 2E cell gives information about the real performance of the carbon material in the practical application of the supercapacitor. Figure 4a shows the cyclic voltammograms for both materials in the 3E cell. These materials behave mostly as double-layer capacitors, as indicated by the almost rectangular shape of the voltammograms, although there is some contribution of pseudocapacitance for ACHG, as evidenced by the small humps at around -0.1 and -0.3 V *vs.* SME on the anodic and cathodic sweeps, respectively. These redox peaks are associated to surface oxygen functionalities, in particular to the quinone-hydroquinone redox couple. [27, 28] This result agrees with the TPD experiments, which showed the presence of quinones/carbonyls (see Figure 3b). On the other hand, ACG shows a high slope at potentials below -0.5 V *vs.* SME in the cathodic sweep, which suggests decomposition of the electrolyte, *i.e.* water reduction. For 1 M H_2SO_4, the electrochemical stability window is between -0.62 and 0.58 V *vs.* SME, though it depends not only on the electrolyte pH, but also on the electrode material used.[27] This is clearly shown here, where water reduction is already observed for ACG at -0.6 V *vs.* SME and not for ACHG. If we continue lowering the potential cut-off down to -1 V *vs.* SME, the electrochemical storage of hydrogen in the narrow microporosity of both materials can be observed (see Figure 4b). Additionally, delayed hydrogen generation/storage can be observed for ACHG, *i.e.* the hump is centered at ~ 0.9 V *vs.* SME whereas for ACG is centered at ~ 0.7 V *vs.* SME, indicating a ~ 200 mV higher overpotential for water decomposition in ACHG than in ACG. This result suggests that ACHG would be highly

suitable as negative electrode in hybrid supercapacitors, allowing for a large enlargement of the voltage window. On the other hand, electro-oxidation of such hydrogen trapped in the pores occurs at a potential higher than the equilibrium potential for ACG, which suggests that hydrogen is strongly trapped in the narrow micropores of ACG and/or that there are important diffusion limitations. Since the size of the micropores is similar in both samples (Figure 2b), we attribute this behavior to a more pronounced tortuosity of the pore network of ACG, compared to ACHG, which may be the result of the higher burn-off of that sample. What is more, the large difference between the positive and the negative current at 0.2 V *vs.* SME in both cases indicates that part of the hydrogen is irreversibly trapped in the pores.

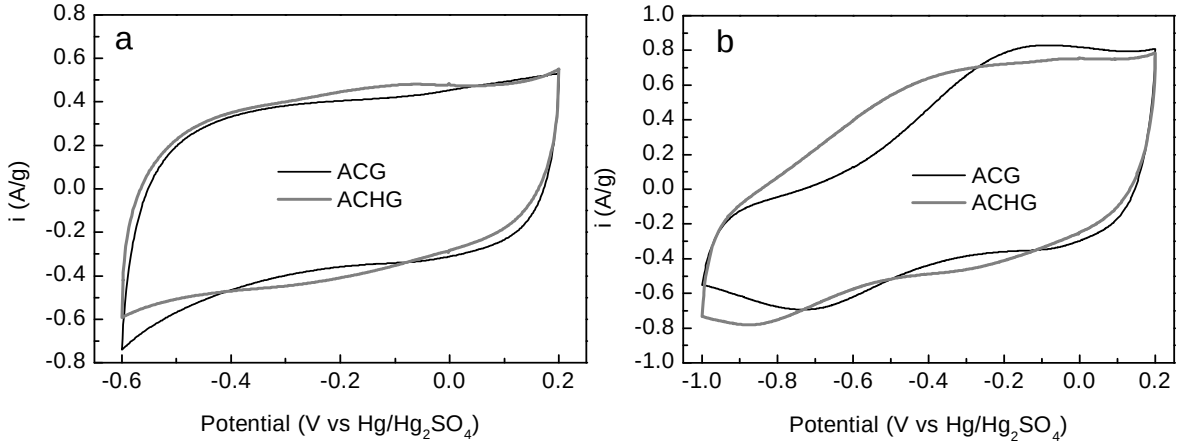

Figure 4. Cyclic voltammograms (3E cell) at room temperature in 1M H_2SO_4 at a scan rate of 2 mV/s: a) potential cut-off at -0.6 V vs. SME and b) potential cut-off at -1 V vs. SME for ACG and ACGH.

The results for the cyclic voltammetry in the 2E cell are shown in Figure 5. Even though ACG exhibits similar PSD to ACHG (see Figure 2b), only ACHG is capable of retaining the rectangular shape characteristic of double-layer capacitors up to 500 mV/s (Figure 5b), indicating fast ion diffusion throughout the porous structure. This behavior agrees with the diffusion limitations observed for the released of hydrogen electrosorbed in the 3E cell. It may also be due to chemical differences existing between

both samples. Indeed, as mentioned in the TPD experiments, high-polarity oxygen groups may slow down the ion transport within the porous network through their interaction with the ion solvated shells.[24] As a result, the capacitance retention of ACHG is superior to that of ACG, as clearly seen in Figure 4c, and also to that of commercial Supra DLC-50. Electrochemical impedance spectroscopy measurements further confirm the favorable performance of ACHG. Thus, the Nyquist plot of ACHG has an insignificant Warburg region at high-medium frequencies (Figure 5d), whereas that of ACG is substantially long, indicating that resistance is encountered by the ions during their migration into the bulk of the electrode particles. Indeed, the value of the equivalent distributed resistance (EDR), determined from the linear projection of the vertical portion at low frequencies to the real axis (subtracting the ESR),[29] is 1.9 Ω for ACG and 0.1 Ω for ACHG. It is worth noting that the equivalent series resistance (ESR), determined from the intercept of the high frequency loop with the real axis, is very similar for both materials (*i.e.* 0.26 Ω for ACG and 0.23 Ω for ACHG), indicating similar conductivity. The higher EDR of ACG in comparison to ACHG brings about a slower frequency response, as shown in the inset in Figure 5d.

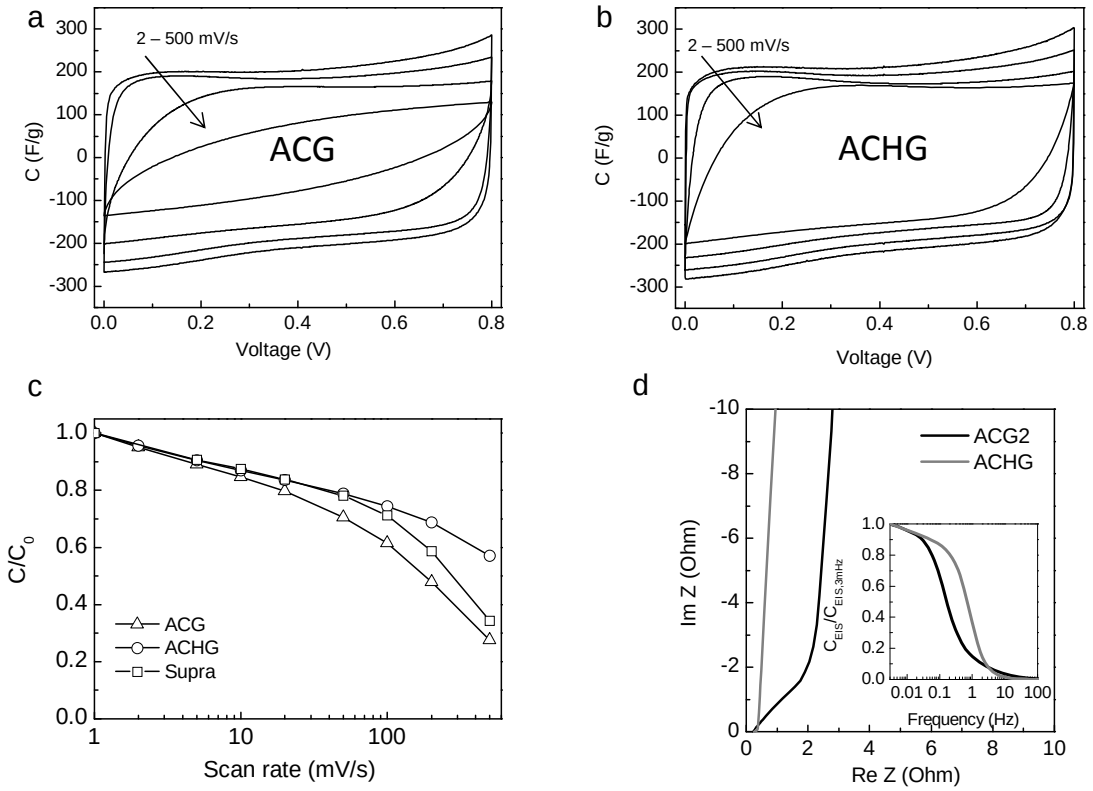

Figure 5. a and b) Cyclic voltammograms (2E cell) at room temperature in 1 M H_2SO_4 at different scan rates (2, 10, 100 and 500 mV/s), c) normalized capacitance retention (C_0 = capacitance at 1 mV/s) vs. scan rate, and d) Nyquist plot (inset: frequency dependence of normalized capacitance) of the different porous carbons.

Galvanostatic charge/discharge experiments were also conducted on the 2E cells prepared with ACG and ACHG. In both cases, the slope of the charge/discharge curves is not constant for low current densities (Figure 6a), which indicates the presence of redox processes. For higher current densities (Figure 6b), larger IR drop (~ twice higher) can be observed for ACG, which agrees with the higher resistance to ions diffusion into the pores observed during the cyclic voltammetry and EIS experiments. This turns out into a poorer rate performance for ACG in comparison to ACHG, as shown in Figure 5c, especially for high discharge rates (> 10 A/g). It is worth highlighting the excellent rate capability of ACHG, whose specific capacitance fades by only 34 % at 90 A/g, so that it still exhibits a high specific capacitance of 155 F/g at

such ultra-high discharge current density. This rate capability is comparable or superior to that of some advanced carbon materials targeted for high-power supercapacitors, such as hierarchical porous graphitic carbon (44 % capacitance fading at 50 A/g, 150 F/g), [30] microporous carbon nanoplates (62 % capacitance loss at 70 A/g, 100 F/g),[31] 3D microporous conducting carbon beehive (45 % capacitance fading at 30 A/g, 140 F/g)[32] or porous graphene-like nanosheets (31 % capacitance loss at 30 A/g, 184 F/g).[33] The specific capacitance of ACHG is higher than that of ACG over the whole range of current densities studied, in accordance to its slightly higher surface area. In both cases, the specific capacitance exceeds 220 F/g (~ 150 F/cm^3 in volumetric units vs. 115 F/cm^3 for Supra DLC-50) for a current density of 0.1 A/g, so that the capacitance per unit of BET surface area is around 15.5 μF/cm^2, value comparable or in many cases superior to activated carbons, [34-38] including hydrothermal carbon-based activated carbons.[10, 39] This is clearly evident when compared to the commercial activated carbon Supra, *i.e.* 8.2 μF/cm^2. The power characteristics of ACHG-based supercapacitor are, as well, superior to those of ACG-based supercapacitor, as evidenced by the Ragone plots depicted in Figure 6d, where ACHG shows a much smaller trade-off between energy and power. In this way, for an energy density of 4 Wh/kg (2.6 Wh/L for ACHG and 2.7 Wh/L for ACG), ACHG exhibits a power density of 1 kW/kg (0.64 kW/L), whereas that of ACG is only 0.2 kW/kg (0.14 kW/L).

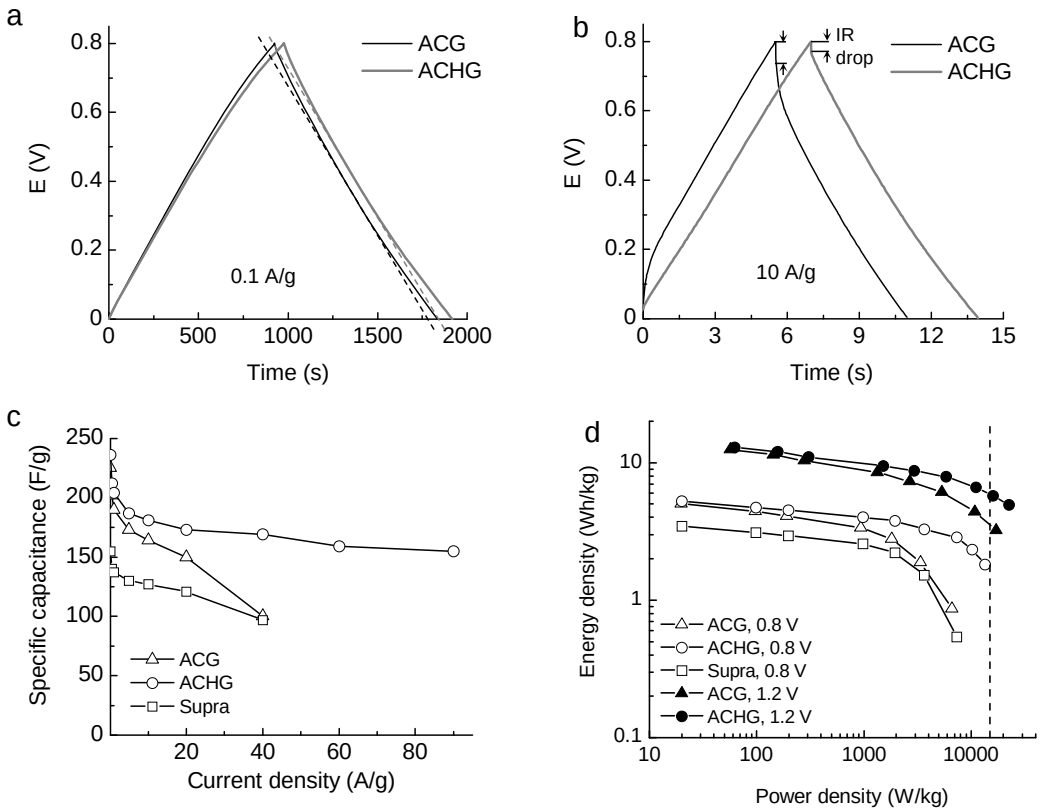

Figure 6. Galvanostatic charge-discharge voltage profiles (2E cell) at 0.1 A/g (a) and 10 A/g (b), rate capability (c) and Ragone plot (d) in 1M H_2SO_4 of the different porous carbons. The vertical dotted line in (d) corresponds to the PNGV power target (15 kW/kg, in terms of electrode active material weight).

Taking into account the voltage stability window of both activated carbons in the 3E cell (Figure 4), an enlargement of the voltage cell was examined in the symmetric 2E cell. The corresponding galvanostatic charge/discharge voltage profiles up to 1.2 V are shown in Figures 7a-b. In both supercapacitors, the voltage profiles are highly symmetric (coulombic efficiency > 97 %) regardless of the maximum voltage but become less linear with the increase in the cell voltage, indicating more pseudocapacitive effects, which are related to the electrochemical storage of hydrogen observed in the 3E cell (Figure 4). In order to confirm that the supercapacitors operate properly at such cell voltages, long-term galvanostatic cycling at 10 A/g was performed successively at 0.8, 1.0, 1.1 and 1.2 V for 10000 cycles at each maximum voltage.

Figures 5b-c prove that both supercapacitors can perfectly withstand voltages up to 1.2 V (*i.e.* the specific capacitance fades by only 4 – 5% and 3 – 5% for ACHG and ACG respectively after 10000 cycles regardless of the cell voltage). These figures show also an increase of specific capacitance with increasing voltage cell as a consequence of the mentioned pseudocapacitive effects. Further confirmation of the robustness of both supercapacitors is provided by EIS. It can be seen in Figure 7f that the Nyquist plot recorded after 40000 cycles for ACHG superimposes to the initial one, evidencing no increase in the internal cell resistance. For ACG (Figure 7e), a slight increase in ESR is observed (0.29 Ω), accompanied by a decrease of EDR (1.3 Ω), as evidenced by a shorter Warburg region, which agrees with the smaller trade-off between energy and power for a voltage cell of 1.2 V in the Ragone plot in Figure 5d. As it can be observed in the Ragone plot, a voltage cell of 1.2 V leads to maximum energy densities of 12.5-13 Wh/kg (~ 8.5 Wh/L) and maximum power densities of 17 kW/kg (11.6 W/L) for ACG and 22.5 W/kg (14.4 W/L) for ACHG. It is worth noting that ACHG-based supercapacitor is able to reach the PNGV (Partnership for a New Generation of Vehicles) power target[30] (see Figure 6d) for a voltage cell of 0.8 V and surpasses it for 1.2 V; however, ACG is only able to reach the PNGC power target using a voltage cell of 1.2 V, but storing almost half the energy of ACHG.

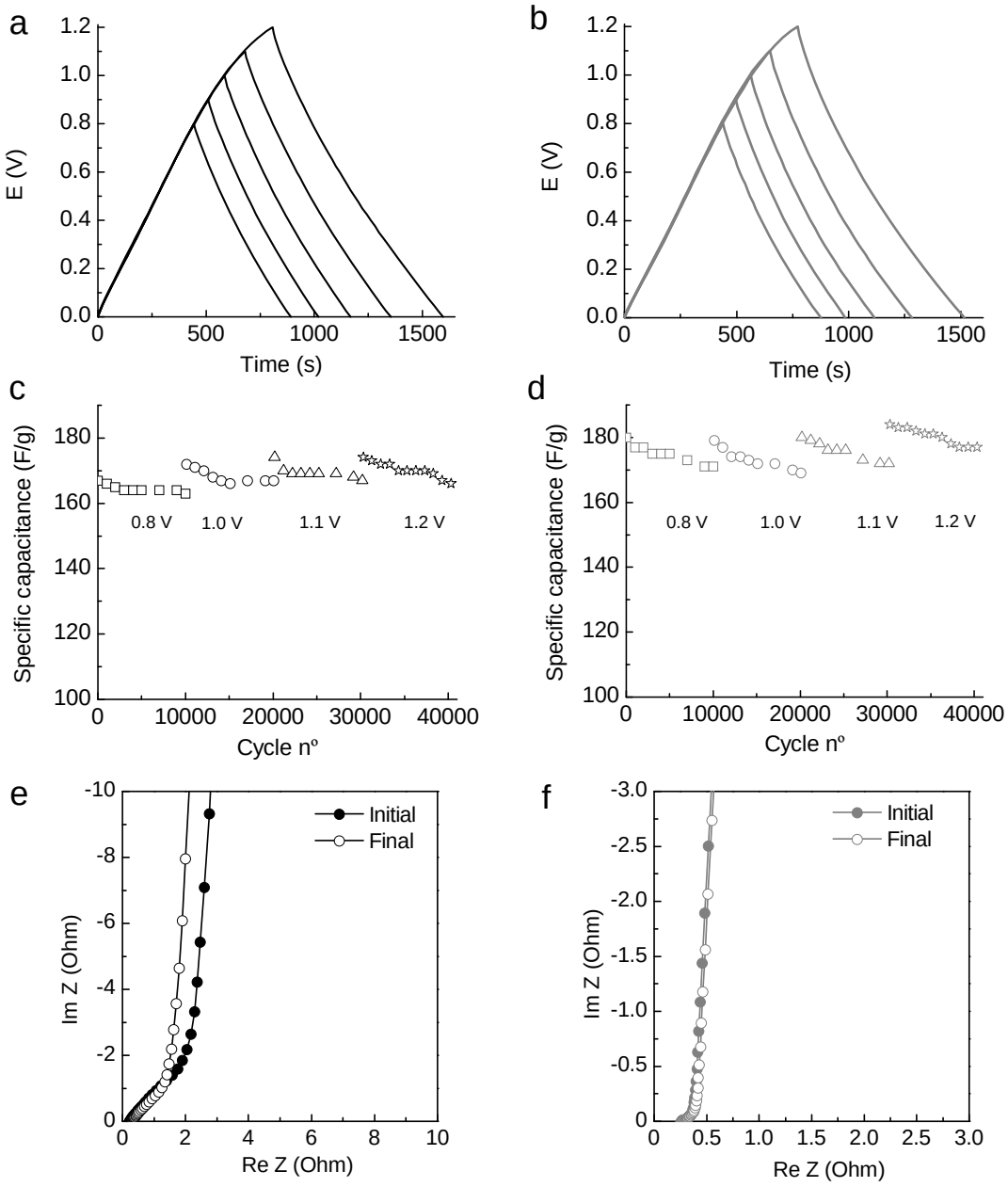

Figure 7. Galvanostatic charge-discharge voltage profiles (2E cell, 0.2 A/g) at increasing voltage cell for ACG (a) and ACHG (b) in 1 M H_2SO_4. Long-term stability at 10 A/g at increasing voltage cell for ACG(c) and ACHG (d). Comparison of the Nyquist plot at the beginning of the testing and after long-term cycling (40000 cycles) for ACG (e) and ACHG (f).

Conclusions

As summary, this work compares the physical, chemical and electrochemical properties of activated carbons produced from glucose and hydrothermally carbonized glucose. The chemical and physical differences existing between them bring about a

different response when tested as electrodes in supercapacitors. Thus, the activated carbon produced from hydrothermally carbonized glucose exhibits a superior rate capability due to the lower EDR, as well as higher specific capacitance in accordance to its slightly higher surface area (~ 240 F/g vs. ~ 220 F/g for glucose-derived activated carbon at 0.1 A/g, ~ 150 F/cm^3). In fact, that rate capability, which leads to a specific capacitance of 155 F/g at 90 A/g, is comparable or superior to that of advanced carbon materials targeted for high-power supercapacitors. Furthermore, both supercapacitors have excellent robustness, even for a large voltage cell of 1.2 V in 1 M H_2SO_4. Thereby, the supercapacitor constructed with the activated carbon produced from hydrothermally carbonized glucose is able to store 4.9 Wh/kg at a power density of 22.5 kW/kg. Additionally, the product yield of the activation process for hydrothermally carbonized glucose doubles that of raw glucose. These results highlight the advantages of applying a hydrothermal treatment to biomass.

Experimental section

Preparation of activated carbons

Glucose and hydrothermally carbonized glucose (30 wt.%, 180°C, 24 h) were chemically activated in a vertical furnace using potassium hydroxide (Sigma-Aldrich) at a temperature of 750ºC and KOH/precursor mass ratio of 2. The samples were labeled ACG and ACHG for glucose and hydrothermally carbonized glucose respectively.

Characterization

Scanning electron microscopy (SEM) images were obtained on a Quanta FEG650 (FEI) instrument. Nitrogen sorption isotherms of the carbon samples were measured at −196 °C using a QUADRASORB SI/MP (Quantachrome Instruments); prior to adsorption measurement, the samples were degassed at 150 °C for 20 h. The apparent

surface area was calculated using the BET method; for the selection of the appropriate relative pressure range, the ISO 9277:2010 was followed. [40] The total pore volume (V_p) was determined from the amount of nitrogen adsorbed at a relative pressure (P/P_0) of 0.95, whereas the micropore volume, V_0, was determined by applying the Dubinin–Radushkevich (DR) equation to the nitrogen isotherm. The pore size distribution (PSD) was determined via a Non-Local Density Functional Theory (NLDFT) method using nitrogen adsorption data, and assuming a slit-shaped pore model.

Elemental chemical analysis was performed using an Elementar vario MICRO cube. The determination of the point of zero charge (pH_{PZC}) was carried out using a modification of the mass titration method described by Noh and Schwarz.[41] Briefly, an adequate mass of carbon is dispersed in a suitable volume of distilled water and stored with constant stirring at room temperature until equilibrium is attained (ca. 24-48 h). Typical carbon/water ratios employed were 1, 2, 4, 6, 8, 10, 12, 14 and 16 %. After equilibrium, the pH value is measured via a glass electrode, and a new aliquot of water is added to the suspension to obtain the next solid/weight fraction. The plateau in the plot of equilibrium pH versus solid weight fraction corresponds to the pH_{PZC} value of the carbon material. The temperature programmed desorption experiments (TPD) were carried out in a chemisorption analyzer (Micromeritics, Autochem II) under and argon flow rate of 50 mL min^{-1}, at a heating rate of 10 ºC min^{-1} up to a final temperature of 1000 ºC. CO and CO_2 evolution was monitored by mass spectrometry (OmniStar 3000).

Electrochemical tests

Electrodes were prepared by mixing 85 wt.% of active material, 10 wt.% of polytetrafluoroethylene (PTFE) binder (Aldrich, 60% suspension in water) and 5 wt.% of Super P (Timcal). The electrochemical measurements were performed in a two- and a three-electrode (2E and 3E, respectively) Swagelok™ type cells. Commercial activated

carbon commonly used in commercial supercapacitors (Supra DLC-50, Norit, S_{BET} = 1890 m^2/g) was analyzed for comparison. For the three-electrode cell configuration, the working electrode was prepared by mixing the active material with the binder and percolator as mentioned above, and using a graphite rod as counter electrode and saturated mercury/mercurous sulfate (SME) as the reference electrode. Regardless of the configuration used, the electrodes were immersed in the electrolyte for 1-2 days before assembling the cell.

The two-electrode capacitors were built using two carbon electrodes of comparable mass and thickness, electrically isolated by glassy fibrous separator. Gold current collectors were used with 1 M H_2SO_4 as electrolyte. The electrochemical characterization was performed using a computer controlled potentiostat (Biologic VMP3 multichannel generator). Cyclic voltammetry was conducted between 0 and 0.8 – 1.2 V at sweep rates ranging from 1 to 500 $mV \cdot s^{-1}$. The specific gravimetric capacitance on one electrode basis obtained in the 2E cell configuration, $C^{sp}_{2E,CV}$ ($F \cdot g^{-1}$), was calculated from the area of the voltammograms by means of the formula:

$$C^{sp}_{2E,CV} = \frac{\oint \mathrm{IdV}}{\nu \cdot \mathrm{m} \cdot \Delta \mathrm{V}} \tag{1}$$

where I = current (A), ν = scan rate (V/s), ΔV = voltage window (V), and m = mass (grams) of carbon material in the working electrode.

Galvanostactic charge/discharge cycling was also performed in the 0 to 0.8 – 1.2 V range, at current densities between 0.05 and 90 $A \cdot g^{-1}$, based on the active mass of a single electrode. The specific gravimetric capacitance on one electrode basis determined from the galvanostatic cycles, $C^{sp}_{2E,GA}$ ($F \cdot g^{-1}$), was calculated by means of the formula:

$$C_{2E,GA}^{sp} = \frac{2\,\mathrm{I}}{(\mathrm{dV/dt})\cdot \mathrm{m}} \tag{2}$$

where *dV/dt* = slope of the discharge curve ($V \cdot s^{-1}$).

Electrochemical impedance spectroscopy (EIS) was performed at open circuit voltage (*i.e.* 0 V) within the frequency range of 3 mHz to 100 kHz and a 10 mV AC amplitude. Nyquist plots and plots of the dependence of the capacitance on frequency were evaluated to characterize the impedance of the tested samples. The specific gravimetric capacitance on one electrode basis, C_{EIS} (F/g), was calculated according to the following formula and normalized with respect to the specific gravimetric capacitance at 3 mHz:

$$C_{EIS} = \frac{2 \cdot \left|\mathrm{Im(Z)}\right|}{2\pi \mathrm{f} \cdot \left[(\mathrm{Im(Z)})^2 + (\mathrm{Re(Z)})^2\right] \cdot \mathrm{m}} \tag{3}$$

where f is the operating frequency (Hz), and Im(Z) and Re(Z) are the imaginary and real components of the total supercapacitor resistance (Ohm).

Acknowledgements

This research work was supported by Spanish MINECO (MAT2012-31651 and CTM2011-23378). M.S. acknowledges the award of the *Ramón y Cajal* contract. M.M. Titirici and Linghui Yu are grateful to the Max-Planck Society for financial support for this project.

References

[1] L. L. Zhang, Y. Gu, X. S. Zhao, *J. Mater. Chem. A*. **2013**, *1*, 9395-9408.
[2] L. Hao, X. Li, L. Zhi, *Adv. Mater.* **2013**, *25*, 3899-3904.
[3] A. Davies, A. Yu, *The Canadian Journal of Chemical Engineering*. **2011**, *89*, 1342-1357.
[4] L. Wei, G. Yushin, *Nano Energy* **2012**, *1*, 552-565.
[5] M. Sevilla, C. Falco, M.-M. Titirici, A. B. Fuertes, *RSC Adv.* **2012**, *2*, 12792-12797.
[6] C. Falco, M. Sevilla, R. J. White, R. Rothe, M. M. Titirici, *ChemSusChem*. **2012**, *5*, 1834-1840.
[7] M. Sevilla, A. B. Fuertes, R. Mokaya, *Energy Environ. Sci.* **2011**, *4*, 1400-1410.
[8] M. Sevilla, A. B. Fuertes, *Energy Environ. Sci.* **2011**, *4*, 1765-1771.

[9] C. Falco, J. P. Marco-Lozar, D. Salinas-Torres, E. Morallón, D. Cazorla-Amorós, M. M. Titirici, D. Lozano-Castelló, *Carbon* **2013**, *62*, 346-355.
[10] C. Falco, J. Manuel Sieben, N. Brun, M. Sevilla, T. van der Mauelen, E. Morallon, D. Cazorla-Amoros, M.-M. Titirici, *ChemSusChem*. **2013**, *6*, 374-382.
[11] L. Wei, M. Sevilla, A. B. Fuertes, R. Mokaya, G. Yushin, *Adv. Energy Mater.* **2011**, *1*, 356-361.
[12] L. Zhao, L.-Z. Fan, M.-Q. Zhou, H. Guan, S. Qiao, M. Antonietti, M.-M. Titirici, *Adv. Mater.* **2010**, *22*, 5202-5206.
[13] L. Zhang, F. Zhang, X. Yang, K. Leng, Y. Huang, Y. Chen, *Small* **2013**, *9*, 1342-1347.
[14] H. Wang, Z. Xu, A. Kohandehghan, Z. Li, K. Cui, X. Tan, T. J. Stephenson, C. K. King'ondu, C. M. B. Holt, B. C. Olsen, J. K. Tak, D. Harfield, A. O. Anyia, D. Mitlin, *ACS Nano* **2013**, *7*, 5131-5141.
[15] C. Falco, F. Perez Caballero, F. Babonneau, C. Gervais, G. Laurent, M. M. Titirici, N. Baccile, *Langmuir* **2011**, *27*, 14460-14471.
[16] J. A. Libra, K. S. Ro, C. Kammann, A. Funke, N. D. Berge, Y. Neubauer, M.M. Titirici, C. Fühner, O. Bens, J. Kern, K.-H. Emmerich, *Biofuels* **2011**, *2*, 71-106.
[17] X. Cao, K. S. Ro, M. Chappell, Y. Li, J. Mao *Energy & Fuels*. **2011**, *25*, 388-397.
[18] P. Makowski, R. Demir Cakan, M. Antonietti, F. Goettmann, M. M. Titirici, *Chem. Commun.* **2008**, 999-1001.
[19] J. A. Macia-Agullo, M. Sevilla, M. A. Diez, A. B. Fuertes, *ChemSusChem* **2010**, 3, 1352-1354.
[20] M.-M. Titirici, R. J. White, C. Falco, M. Sevilla, *Energy Environ. Sci.* **2012**, *5*, 6796-6822.
[21] M. C. Rillig, M. Wagner, M. Salem, P. M. Antunes, C. George, H.-G. Ramke, M.-M. Titirici, M. Antonietti, *Appl Soil Ecol.* **2010**, *45*, 238-242.
[22] J. L. Figueiredo, M. F. R. Pereira, M. M. A. Freitas, J. J. M. Órfão, *Carbon* **1999**, *37*, 1379-1389.
[23] J. L. Figueiredo, M. F. R. Pereira, *Catal. Today* **2010**, *150*, 2-7.
[24] Y. R. Nian, H. Teng, *J. Electroanal. Chem.* **2003**, *540*, 119-127.
[25] C. T. Hsieh, H. Teng, *Carbon* **2002**, *40*, 667-674.
[26] L. Yu, C. Falco, J. Weber, R. J. White, J. Y. Howe, M.-M. Titirici, *Langmuir* **2012**, *28*, 12373-12383.
[27] M. P. Bichat, E. Raymundo-Piñero, F. Béguin, *Carbon* **2010**, *48*, 4351-4361.
[28] E. Raymundo-Piñero, M. Cadek, F. Béguin, *Adv. Funct. Mater.* **2009**, *19*, 1032-1039.
[29] R. Kötz, M. Carlen, *Electrochim. Acta* **2000**, *45*, 2483-2498.
[30] D.-W. Wang, F. Li, M. Liu, G. Q. Lu, H.-M. Cheng, *Angew. Chem. Int. Ed.* **2008**, *47*, 373-376.
[31] Y. S. Yun, S. Y. Cho, J. Shim, B. H. Kim, S.-J. Chang, S. J. Baek, Y. S. Huh, Y. Tak, Y. W. Park, S. Park, H.-J. Jin *Adv. Mater.* **2013**, *25*, 1993-1998.
[32] D. Puthusseri, V. Aravindan, S. Madhavi, S. Ogale, *Energy Environ. Sci.* **2014**, *7*, 728-735.
[33] L. Sun, C. Tian, M. Li, X. Meng, L. Wang, R. Wang, J. Yin, H. Fu, *J. Mater. Chem. A* **2013**, *1*, 6462-6470.
[34] V. Ruiz, C. Blanco, R. Santamaría, J. M. Ramos-Fernández, M. Martínez-Escandell, A. Sepúlveda-Escribano, F. Rodríguez-Reinoso, *Carbon* **2009**, *47*, 195-200.
[35] T. A. Centeno, F. Stoeckli, *Electrochim. Acta* **2006**, *52*, 560-566.
[36] K. Kierzek, E. Frackowiak, G. Lota, G. Gryglewicz, J. Machnikowski, *Electrochim. Acta* **2004**, *49*, 515-523.
[37] L. Wei, G. Yushin, *Carbon* **2011**, *49*, 4830-4838.
[38] M. Olivares-Marín, J. A. Fernández, M. J. Lázaro, C. Fernández-González, A. Macías-García, V. Gómez-Serrano, F. Stoeckli, T. A. Centeno, *Mater. Chem. Phys*. **2009**, *114*, 323-327.
[39] L. Wang, Y. Guo, B. Zou, C. Rong, X. Ma, Y. Qu, Y. Li, Z. Wang, *Biores. Technol*. **2011**, *102*, 1947-1950.
[40] in ISO 9277:2010. Determination of the specific surface area of solids by gas adsorption - BET method. Second Edition of ISO 9277, **2012**.

[41] J. S. Noh, J. A. Schwarz, *J. Colloid Interface Sci.* **1989**, *130*, 157-164.